*remote sensing*

MDPI

*Article*

# Polar Sea Ice Detection Using a Rotating Fan Beam Scatterometer

**Liling Liu [1,*], Xiaolong Dong [2], Wenming Lin [3] and Shuyan Lang [4]**

[1] School of Artificial Intelligence, China University of Mining and Technology-Beijing, Beijing 100083, China
[2] The CAS Key Laboratory of Microwave Remote Sensing, National Space Science Center, Chinese Academy of Sciences, Beijing 100190, China; dongxiaolong@mirslab.cn
[3] School of Marine Sciences, Nanjing University of Information Science & Technology, Nanjing 210044, China; wenminglin@nuist.edu.cn
[4] National Satellite Ocean Application Service, Beijing 100081, China; langshuyan@mail.nsoas.org.cn
* Correspondence: liulilling@cumtb.edu.cn

**Abstract:** Scatterometers are dedicated to monitoring sea surface wind vectors, but they also provide valuable data for polar applications. As a new type of scatterometer, the rotating fan beam scatterometer delivers a higher diversity of incidence angles and more azimuth sampling. The paper takes the first rotating fan beam scatterometer, the China France Oceanography Satellite scatterometer (CSCAT), as an example to explore the effectiveness of this new type of scatterometer in polar sea ice detection. In this paper, a Bayesian method with consideration of geometric characteristics of CSCAT is developed for sea ice detection. The implementation of this method includes the definition of CSCAT backscatter space, an estimation of the sea ice Physical Model Function (GMF), a calculation of the sea ice backscatter distance to the sea ice GMF, a probability distribution function (PDF) estimation of the square distance to the GMF (sea ice GMF and wind GMF), and a calculation of the sea ice Bayesian posterior probability. This algorithm was used to generate a daily CSCAT polar sea ice mask during the CSCAT mission period (2019–2022) (by setting a 55% threshold on the Bayesian posterior probability). The sea ice masks were validated against passive microwaves by quantitatively comparing the sea ice edges and extents. The validation suggests that the CSCAT sea ice edge and extent show good agreement with the sea ice concentration distribution (i.e., sea ice concentration $\geq$ 15%) of the Advanced Microwave Scanning Radiometer 2 (AMSR2). The average Euclidean distance of the sea ice edges was basically less than 12.5 km, and the deviation of the sea ice extents was less than $0.3 \times 10^6$ km$^2$.

**Keywords:** scatterometer; CSCAT; sea ice detection; Bayesian algorithm



**Citation:** Liu, L.; Dong, X.; Lin, W.; Lang, S. Polar Sea Ice Detection Using a Rotating Fan Beam Scatterometer. *Remote Sens.* **2023**, *15*, 5063. https://doi.org/10.3390/rs15205063

Academic Editor: Yi Luo

Received: 18 September 2023
Revised: 14 October 2023
Accepted: 17 October 2023
Published: 21 October 2023



## 1. Introduction

Sea ice is not only a critical input variable for the global climate models but also a relevant ancillary parameter for the accurate retrieval of ocean surface wind data [1]. The polar ocean region is mainly composed of sea ice and open water. Polar sea ice accounts for a large proportion of the global sea ice. Therefore, the study of the spatial and temporal properties of polar sea ice is of great significance. In the past and in the present, numerous spaceborne instruments have been employed for research and the monitoring of polar ocean regions, among which satellite scatterometers have proven to be extremely valuable in observing polar regions with the advantages of rapid repeat coverage, a relatively high spatial resolution, and a low sensitivity to the complex atmospheric effects [2].

Scatterometers are active microwave systems that are commonly used for ocean applications, such as ocean surface wind retrieval and sea ice monitoring. The radar backscattering principle over the open water is defined by Bragg scattering, as such scatterometers take advantage of the relationship between the radar backscattering signal and the sea surface winds to determine ocean surface wind speed and direction. However, the microwave backscattering from sea ice is a combination of both volume and surface scattering, which

depends on the observing geometry, the electrical properties, and the physical characteristics of sea ice [3]. The remarkable difference between the sea ice backscattering signal and the open water backscattering signal is the basis for sea ice and open water discrimination.

Continuous monitoring of the sea ice in polar regions has been done using many scatterometers, such as the C-band scatterometers on the Europe Remote Sensing (ERS) satellites, the Advanced scatterometer (ASCAT) onboard MetOp satellite series, and the Ku-band pencil beam scatterometers like QuikSCAT and OSCAT [1]. The C-band scatterometers are with fixed fan beams, such that measurements are collected over a wide range of incidence angles (typically ~20° to 60°), and a fixed number of azimuthal looks are acquired. Moreover, only one single polarization (i.e., vertical polarization (VV)) is available for the past C-band scatterometers. The Ku-band pencil beam scatterometers generally employ a rotating antenna to collect measurements at two different incidence angles and two diverse azimuth angles via VV and horizontal polarization (HH) beams. Both types of radar scatterometers have their advantages and disadvantages in terms of polar sea ice monitoring.

Since 2018, a third type of scatterometer, namely a rotating fan beam scatterometer, has been operated in space. Compared with the existing fixed fan beam and rotating pencil beam scatterometers, the rotating fan beam scatterometer presents several new characteristics. That is, compared to a fixed fan beam scatterometer, it does not have a nadir gap, and compared to a rotating pencil beam scatterometer, it has more individual backscatter observations in a wind vector cell (WVC) [4]. Therefore, a higher diversity of incidence angles and more azimuth sampling are available from the rotating fan beam scatterometers than the prior systems, which enables better research on sea ice scattering mechanisms. This opens up opportunities for improving sea ice monitoring and expanding polar sea ice monitoring records using this new scatterometer. In the past few years, the Royal Netherlands Institute of Meteorology (KNMI) and Ocean and Sea Ice Satellite Application Facility (OSI SAF) have provided consistent long-term records of sea ice monitoring from satellite scatterometry (ERS, QuikSCAT, ASCAT, and OSCAT) dating back from 1992 to 2017 [5]. The investigation of sea ice detection with the rotating fan beam scatterometer will contribute to the long-time series of scatterometer sea ice monitoring, providing a valuable baseline for the studies of polar regions.

The rotating fan beam scatterometer is unique in terms of antenna mechanisms among currently operating scatterometers, but it also poses challenges to sea ice detection algorithms. To date, there are two rotating fan beam scatterometers, namely the China French Ocean Satellite (CFOSAT) scatterometer (CSCAT) and the Fengyun-3E Wind Radar (WindRad) [4,6]. Both the CSCAT and WindRad adopt dual polarization (HH and VV), but they have some different characteristics. The CSCAT is a dual antenna system operating in the Ku band, while the WindRad has four fan beams, two of which operate in the C band and the other two in the Ku band. This article takes CSCAT as an example to explore the effectiveness of this new scatterometer in polar sea ice detection.

At present, the sea ice detection (or sea ice and open water discrimination) methods for satellite scatterometers are mainly classified into two different types, i.e., the physics-based methods and the machine-learning-based methods [7,8]. Both are based on the contrasting scattering properties between sea ice and open water. Given that the CSCAT is unique among the current operational scatterometers in terms of its observation geometry, we focus on the physical method in this paper. There are two kinds of physics-based sea ice detection algorithms. The first one is the BYU algorithm proposed by Long et al. [9,10]. This algorithm is based on a maximum likelihood discriminant scheme, using sea ice/open water clustering centroids and covariance matrices as inputs. The centroid of sea ice/open water star clusters is determined in the transformation space of the pseudo polarization, average backscattering, and azimuth changes. Although the BYU algorithm is expected to perform well under calm and winter conditions, its seasonal performance has not been fully validated [11]. The second one is the KNMI algorithm proposed by Belmonte Rivas et al. [12–14]. The KNMI algorithm is based on the maximum

posterior (Bayesian) framework, which uses prior information from sea ice and open water, as well as the conditional probability of the square distances (i.e., residual) between the radar measurements and sea ice or open water Geophysical Model Functions (GMFs). Overall, the KNMI algorithm is able to reach the theoretical capability of sea ice discrimination by accounting for the scatterometer noises. We have applied the KNMI algorithm of QuikSCAT to the CSCAT by only using the data at an incidence angle of 40° for sea ice detection [15,16]. Li et al. adapt the Bayesian method for the CSCAT following their previous implementations of the KNMI algorithm for ERS and ASCAT [17]. In this paper, the KNMI algorithm is further adjusted for the CSCAT sea ice detection by taking the characteristics (diverse incidence angles and azimuth sampling) of the rotating fan beam scatterometer system into account.

Section 2 introduces the observational geometry and scientific products of the CSCAT. Section 3 presents the details of the sea ice detection algorithm of the CSCAT. Section 4 presents the results and discussion, including the sea ice mapping and quantitative comparison of passive microwave sea ice concentrations on the sea ice edge and sea ice extent. Section 5 summarizes our results.

## 2. CSCAT on CFOSAT

The CSCAT is operated at the Ku-band microwave frequency with a central frequency of 13.256 GHz. It has two antenna beams, i.e., one vertically (V) polarized fan beam and one horizontally (H) polarized fan beam. The conical scanning mechanism of the CSCAT allows for a continuous observation swath of 1000 km, such that it is able to provide a global coverage of the Earth's surface in three days.

### *2.1. Geometry of Observation*

The CSCAT uses two 1.2 m slotted waveguide antennas to generate two fan beams (i.e., VV and HH) that sweep the Earth's surface conically at intermediate incidence angles (28°–51°). Given the orbital altitude of about 520 km, the footprint size of each beam is about 260 km × 10 km. In scatterometry, the radar transmits linear frequency modulated pulses and then receives the backscattered signals using a dechirp module and a Fast Fourier Transformer to provide sub-footprint range gates (namely slices). The CSCAT generates 40 slices with a range resolution of 10 km, among which about 26 slices are valid for wind inversion and sea ice monitoring [18].

Due to the geometry of the rotating fan beam, the CSCAT generates a large overlap within the swath and provides a large amount of backscatter (i.e., $\sigma^0$) acquisition for a single surface resolution cell (or WVC). For each orbital pass, the CSCAT wind processor generates 42 WVCs on a resolution of 25 km × 25 km in the 1000 km swath. Correspondingly, the WVC is numbered according to the position of the subsatellite cross track, where WVC 1 is located in the leftmost swath and WVC 42 is located in the rightmost swath. Each WVC registers 2–8 views for both VV and HH beams. The observation geometry of the CSCAT is shown in Figure 1.

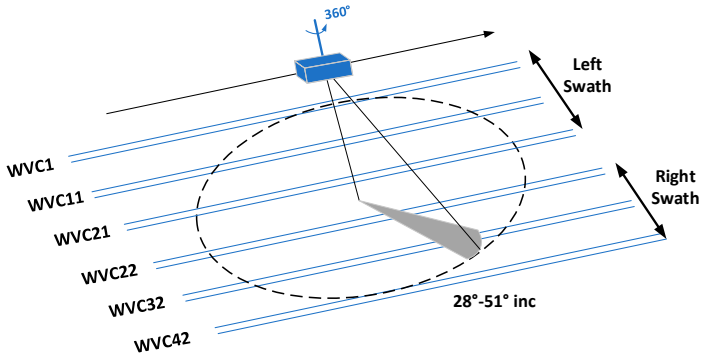


**Figure 1.** Observation geometry of CSCAT.

### *2.2. Scientific Product Specification of CSCAT*

The operation ground processor of the CSCAT is developed by the National Satellite Ocean Application Service Center (NSOAS) of China. The following data products are generated by the processing chain and are accessible to users [19].

(1) L1B data include the time ordered slices $\sigma^0$ and slice geolocations.
(2) L2A data include the average backscatter value of each WVC (usually with a resolution of 25 km), and each WVC obtains 2–8 views of each antenna beam.
(3) L2B data include the sea surface wind information.

In our study, L2A and L2B data are used for the sea ice detection. The data files are all in NetCDF format. The data structure within the L2A/2B package is formed on the basis of the row number (along track) and the WVC number (across track).

## 3. Sea Ice Detection Algorithm of CSCAT

The KNMI sea ice detection algorithm is based on the Bayesian framework. In this section, a Bayesian method considering multiple incidence angles and the dual polarizations of the CSCAT is derived. The implementation of this method includes the CSCAT backscatter space definition, the sea ice GMF estimation, the calculation of the sea ice backscatter distance to the sea ice GMF, the probability distribution function (PDF) estimation of the square distances to GMFs (sea ice GMF and wind GMF), and the sea ice Bayesian posterior probability calculation.

The KNMI algorithm projects the scatterometer measurements onto the polar stereo projection map of the National Snow and Ice Data Center (NSIDC) [20]. For the sake of validation, the CSCAT L2 data are resampled onto the polar ice maps with a grid resolution of 12.5 km × 12.5 km. The dimension of the sea ice map is 896 × 608 and 664 × 632 for the North and South polar regions, respectively. Figure 2 shows the coverage maps of the NSIDC Polar Stereographic Projection. The overlying black boxes are the sea ice mapping areas. In the following study, the backscatter data on the NSIDC polar stereographic projection maps are used for sea ice detection.

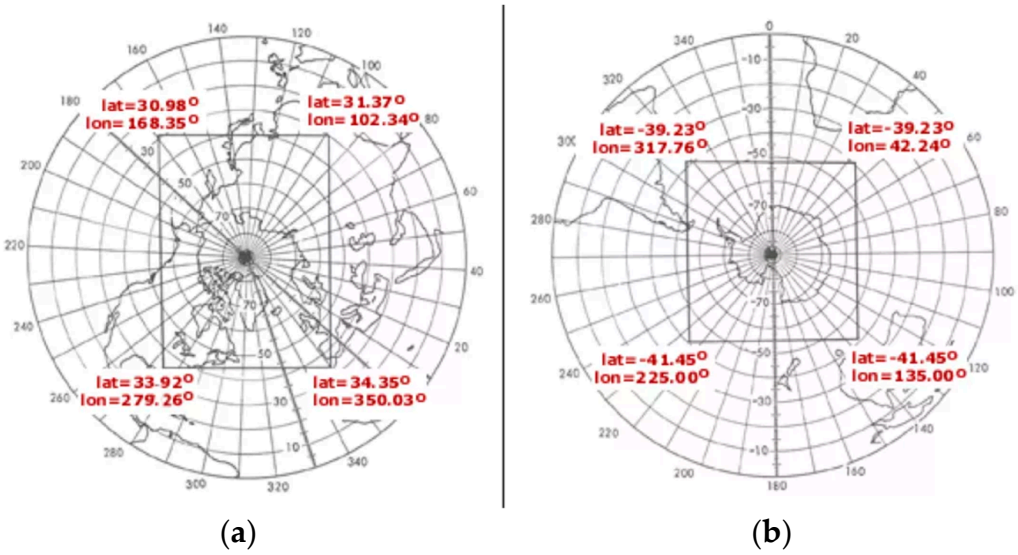


**Figure 2.** NSIDC Polar Stereographic Projection coverage maps: (**a**) North Pole; (**b**) South Pole.

### *3.1. CSCAT Backscatter Space*

The first part of this section defines the CSCAT backscatter space for the sake of analysis. According to the observed geometry of the CSCAT, a set of 4–16 backscatter views is obtained for each WVC. Usually, each WVC registers 2–8 VV/HH measurements (i.e., $[\sigma^0_{VV}, \sigma^0_{HH}]$ ) with different incidence and azimuth angles. The measurements of $[\sigma^0_{VV}, \sigma^0_{HH}]$ share similar azimuth angles [4]. Therefore, the CSCAT backscatter space can be defined

by several two-dimensional (2D) plots consisting of polarization measurement pairs. Each $[\sigma^0_{VV}, \sigma^0_{HH}]$ is separated by different incidence angles, and the range of incidence angles (or number of pairs) for each WVC depends on its position. The backscatter distribution of the sea ice and open water is investigated in the defined CSCAT backscatter space.

Figure 3 shows the backscatter distribution of the sea ice and open water measured in WVC 15 for the North and South Poles on 15 January 2019. Here, the land flags in the L2A dataset are used to exclude land points. The ice flags from the L2 dataset are used to determine ice observations. If the backscatter observations are linked to negative ice flags and the number of wind ambiguity solutions in the corresponding WVC is greater than zero, the WVC is judged as ocean water. It is noted that sea ice and open water occupy significantly different areas. For the same incident angle, open water is generally has a characteristic of $\sigma^0_{VV} > \sigma^0_{HH}$, but the sea ice results in a depolarized measurement, i.e., $\sigma^0_{VV} \approx \sigma^0_{HH}$, and stronger echoes in the measurements. This is due to the fact that open water backscattering is dominated by the short capillary gravity waves, which normally result in a substantial polarization ratio ($\sigma^0_{VV}/\sigma^0_{HH}$). In addition, for open waters, the azimuthal response of backscattering is anisotropic, but for sea ice, it is isotropic [12]. Therefore, the distinct incidence, polarization, and azimuthal properties of sea ice allow for its effective identification against open water.

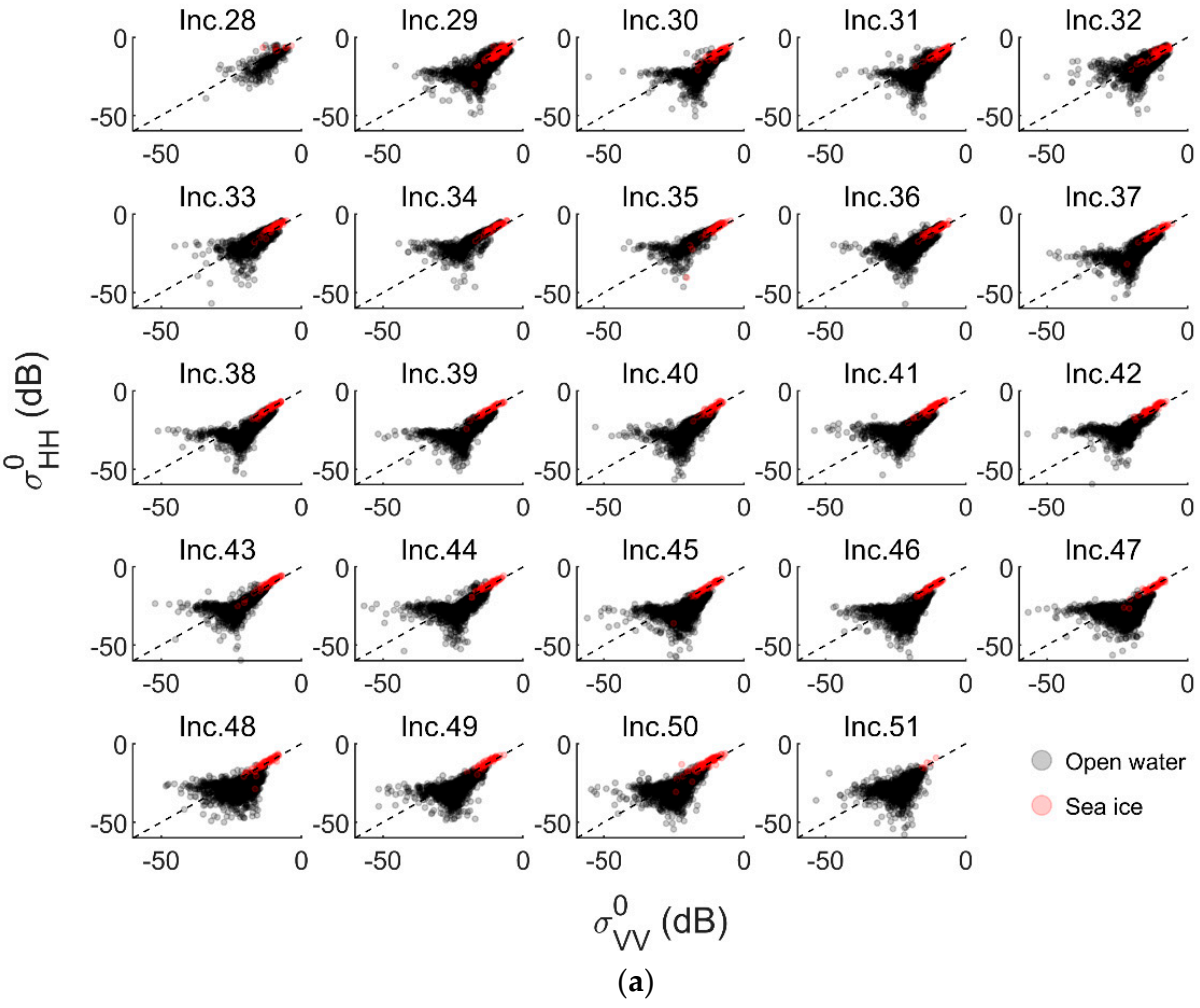


(**a**)

**Figure 3.** *Cont.*

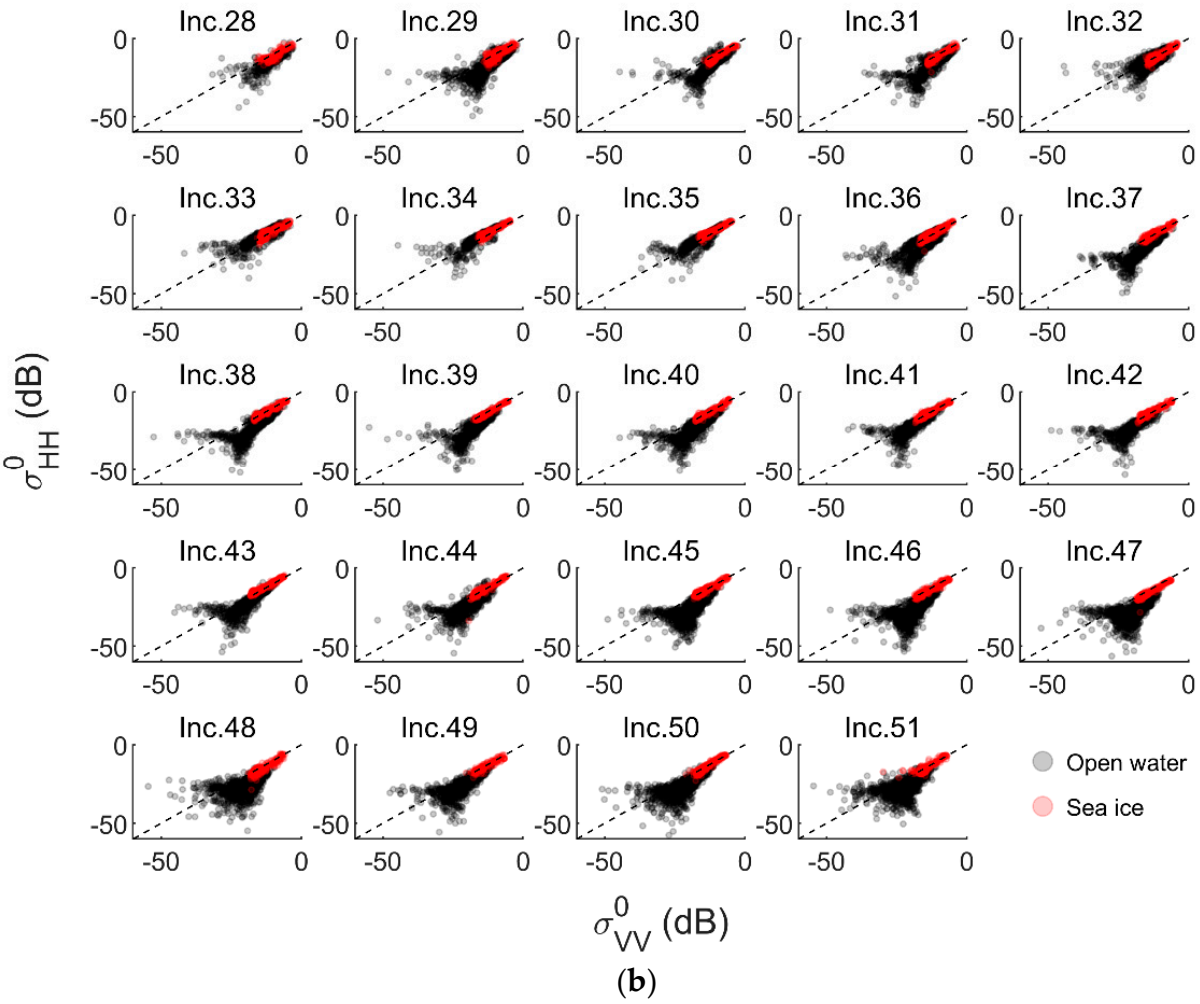


**Figure 3.** Measured backscatter distributions of sea ice and open water for WVC 15 in the CSCAT backscatter space on 15 January 2019: (**a**) North Pole; (**b**) South Pole.

### *3.2. GMF for Sea Ice*

The GMF is an empirically derived function that relates surface conditions to the backscatters observed from various incident angles, azimuth angles, and polarizations. As such, the GMF describes backscatter data as a function of physical and observational parameters, which in turn are used for wind retrieval in open water. Specifically, the GMF of wind is naturally dominated by two physical parameters (wind speed and direction) and three observational parameters (incidence angle, azimuth angle, and polarization). For the CSCAT, the NSCAT-4 GMF is adopted for ocean wind retrieval [19]. Though there is not a mature sea ice GMF for the Ku-band fan beam scatterometer, it can be developed similarly to the wind GMF and then applied to sea ice retrieval.

There are various types of sea ice, such as sea ice containing a certain amount of saline water, sea ice covered by snow, and sea ice formed in different layers due to the melting and refreezing processes [3]. Different types of sea ice have different backscattering characteristics. Therefore, it remains unknown how many physical parameters can be used to define the sea ice backscattering. However, the examination of the backscatter distribution of the sea ice with the CSCAT backscatter space (as shown in Figure 3) indicates that all sea ice samples with similar incidence angles lie along a straight line in the 2D $\sigma_0$ (dB) space. This is consistent with the depolarization characteristic of the sea ice.

In this case, we can describe the GMF of sea ice using a 1D linear model, which has two parameters (slope and intercept) for each incident angle of the CSCAT.

$$\sigma^0_{HH} = Slope \times \sigma^0_{VV} + Intercept \quad (1)$$

Using this assumption, the GMF of sea ice can be derived from the observed sea ice backscatter of the CSCAT. The GMF parameters (slope and intercept) of the sea ice are obtained daily for a year. Figures 4 and 5 show the CSCAT sea ice GMF parameters for different WVCs in the North and South Poles in 2019.

In these figures, 'W', 'Sp', 'Su', and 'F' represent winter, spring, summer, and fall throughout the year. The four seasons refer to the local seasons in the polar regions, where summer in the southern hemisphere is winter in the northern hemisphere, and so on. In the North Pole, the sea ice GMF parameters of the CSCAT for all WVCs are very stable during the winter, except for incidence angles of 28° and 51°. In contrast, there are significant fluctuations associated with the sea ice GMF parameters in the summer months. This is because the melting of sea ice, especially in the first year, changes rapidly with increasing temperatures. In addition, the obvious fluctuations appear in late spring and early fall as well, since the sea ice starts to melt in late spring and the temperature in early fall is still high enough to prevent the sea ice from freezing. In early to middle spring and middle to late fall, the sea ice GMF parameters are relatively stable for all incidence angles except for 28° and 51°. In the South Pole, there are noticeable fluctuations of the sea ice GMF parameters in summer, early fall, and late spring periods, as well as in the North Pole. Moreover, similar to the North Pole, the sea ice GMF parameters for the incidence angles from 29° to 50° present smaller fluctuations than the other incidence angles, notably during the winter period.

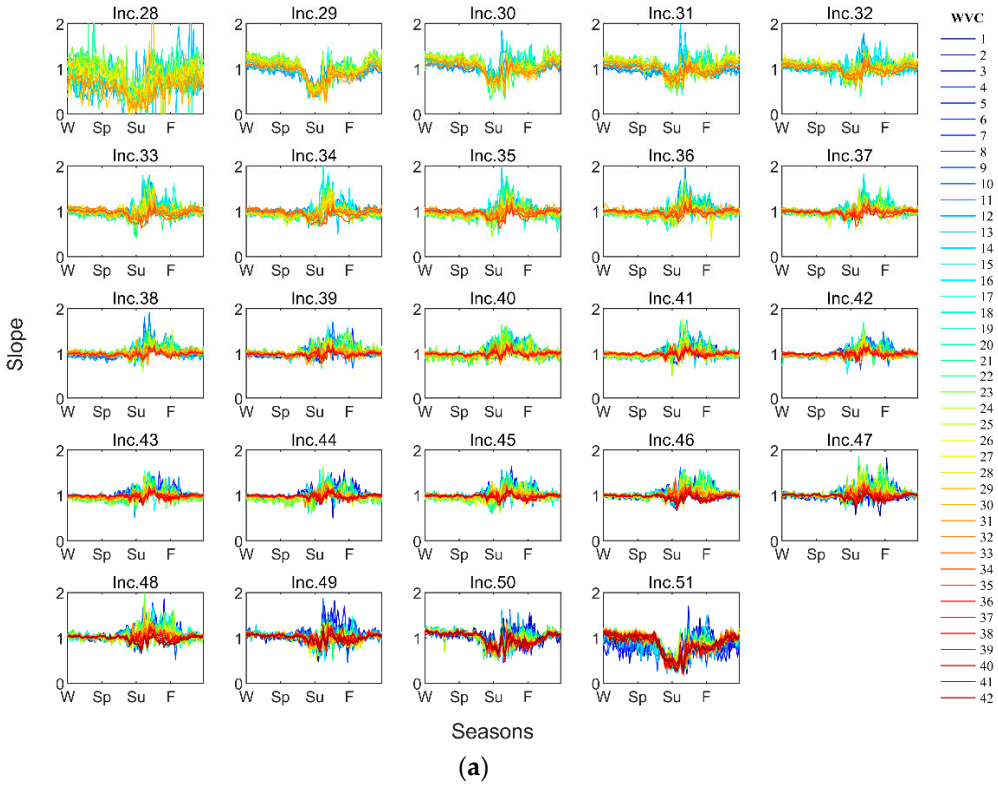


(**a**)

**Figure 4.** *Cont.*

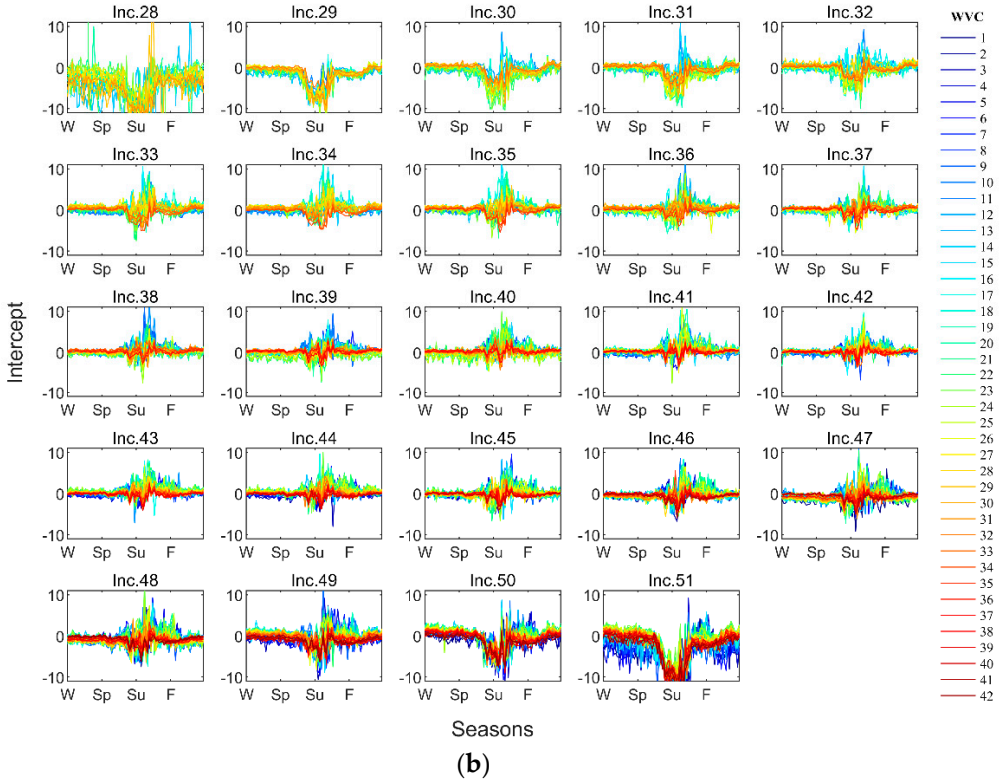


(**b**)

**Figure 4.** Sea ice GMF parameters of CSCAT for different WVCs in North Pole in 2019: (**a**) slope; (**b**) intercept.

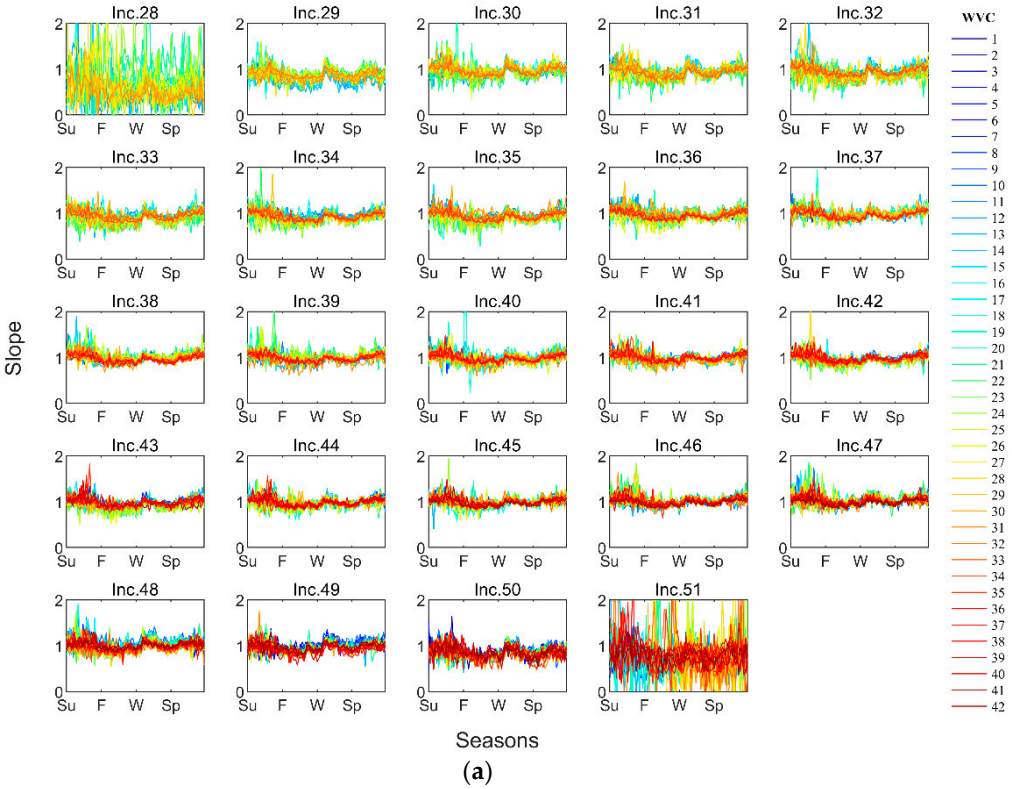


(**a**)

**Figure 5.** *Cont.*

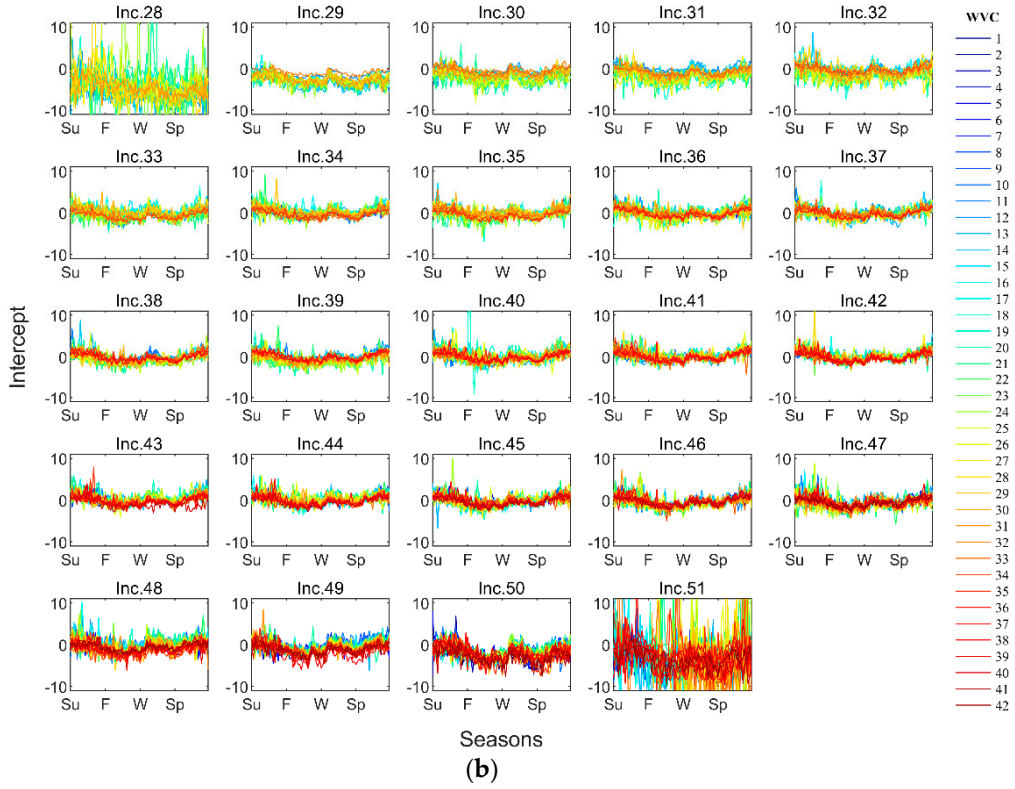


(**b**)

**Figure 5.** Sea ice GMF parameters of CSCAT for different WVCs in South Pole in 2019: (**a**) slope; (**b**) intercept.

Based on the above analysis, we note that the variation in the sea ice GMF parameters at different WVCs is small for the same incident angle (except for 28° and 51°). Therefore, the statistical knowledge about the CSCAT sea ice GMF can be obtained by using the sea ice backscatter points of all WVCs for the same incident angle. Since the sea ice GMF parameters at 28° and 51° are unstable, the range of incidence angles from 29° to 50° are applied for sea ice detection of the CSCAT. Figure 6 shows the sea ice GMF parameters of the CSCAT for different incidence angles in 2019.

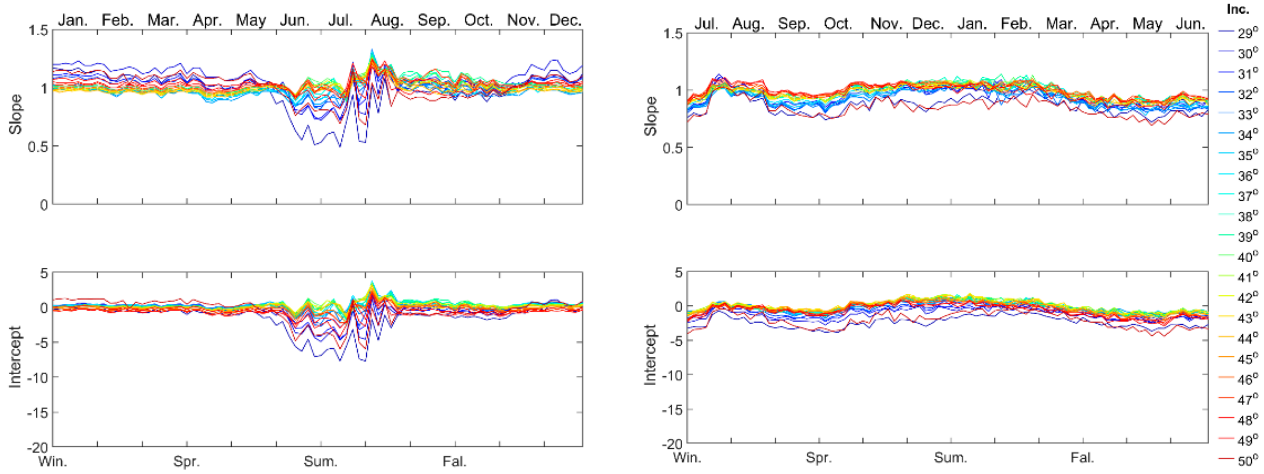


(**a**) (**b**)

**Figure 6.** Sea ice GMF parameters (slope and intercept) of CSCAT for different incidence angles in 2019: (**a**) North Pole; (**b**) South Pole.

It is noted that, in the North Pole, except for in June, July, and August, the GMF parameters of the sea ice at each incident angle usually do not change significantly in different seasons. The parameters of the three months show a negative bias with respect to the other months due to the presence of a mixed ice–water sea state. Besides, the slope and intercept for incident angles of 29° and 50° have the greatest variation. While in the South Pole, the GMF parameters of the sea ice at various incident angles vary relatively little throughout the year, and the parameters corresponding to incident angles of 29° and 50° have the greatest deviation from the other incident angles. In addition, the slopes of the sea ice GMF in the South Pole are generally smaller than those in the North Pole. This is because the largest backscatter of the South Pole arises from the ice shelves rather than multiyear sea ice, with the former generally corresponding to a large polarization ratio of $\sigma^0_{HH}/\sigma^0_{VV}$. In general, the parameters of sea ice GMF are more stable for the South Pole. The reason for this is that most of the floating sea ice disappears in the summer, such that the backscatter from the ice shelves and mixed ice–water pixels dominates the distribution of sea ice points in the South Pole. Considering the parameter changes for incidence angles of 29° and 50°, a range of incidence angles of 30°–49° is ultimately selected to detect sea ice in the CSCAT.

To ensure the uniformity of the CSCAT sea ice GMF, we take the mean winter distribution in the North Pole as the most representative pure ice backscatter throughout the year, and then use it for the CSCAT sea ice GMF. The incidence angle range is 30°–49°, which is suitable for the sea ice detection by the CSCAT. The CSCAT sea ice GMF with an incidence angle of 30°–49° from 2019 to 2022 is shown in Figure 7. It is obvious that the slope curves for 2019, 2020, and 2022 basically overlap, especially when the incidence angle is between 32° and 47°, with a slope value close to 1. However, the results for 2021, with a mean slope value of about 0.9, slightly deviate from the other three years. This may be due to the calibration problem during the operational period of the CSCAT.

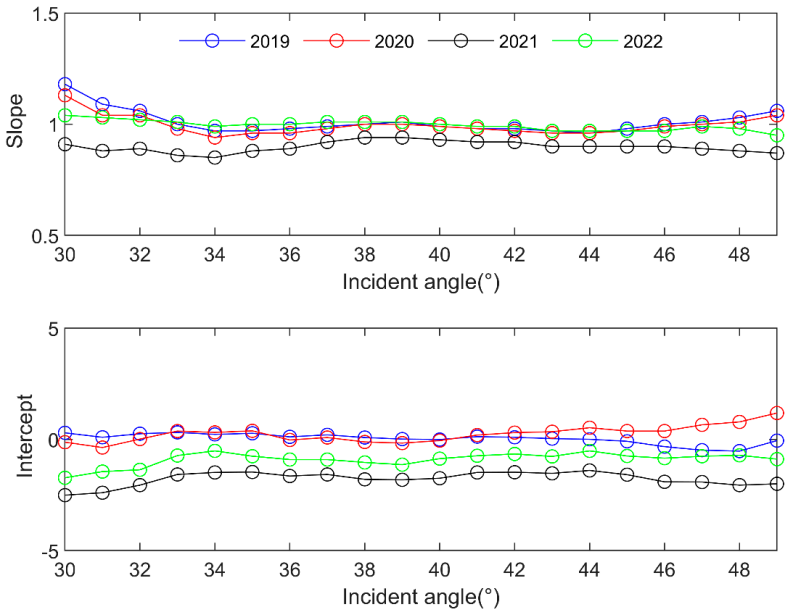


**Figure 7.** Sea ice GMF parameters (slope and intercept) of CSCAT for incidence angles of 30°–49°.

The intercept parameters for 2019 and 2020 are basically the same between incidence angles of 32° to 41°, and the values are approximately equal to 0. As the incident angle increases, the difference between the two curves also increases, typically to a value within 0 to 1. However, the intercept parameter for 2021 has the largest absolute value (around 3), followed by the result in 2022 (about 2).

### *3.3. Backscatter Distances to Sea Ice GMF*

Due to the KNMI algorithm requiring the distance from the sea ice measurement to its GMF, the backscatter distance from the sea ice to the linear ice GMF model is first analyzed. Taking the North Pole on 15 January 2019 as an example, the histograms of sea ice backscatter distances from four selected incident angles (30°, 36°, 42°, 49°) to the sea ice GMF are shown in Figure 8. Due to the distribution being close to Gaussian, the histogram is fitted by a Gaussian function with specific deviations and standard deviations (i.e., std). In this way, the Gaussian curve (red line) and its histogram contour (black line) are superimposed. And the corresponding Gaussian bias and std values are explicated in the figure. Generally, the Gaussian fitting is effective. However, there are some non-overlapping pixels caused by mixed ice–water pixels.

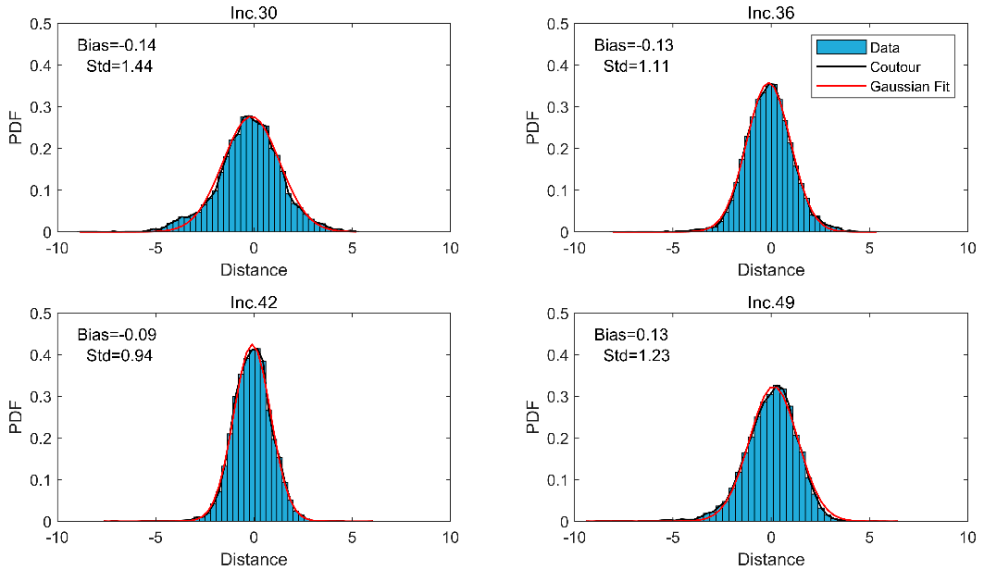


**Figure 8.** The distribution of sea ice backscatter distances to the sea ice GMF (North Pole, 15 January 2019).

The Gaussian curves of the distance between the sea ice backscatter and its GMF backscatter for different incident angles of the CSCAT are shown in Figure 9. We note that the bias and standard deviation values are different for these curves. For most incident angles, the Gaussian curves corresponding to the South Pole are similar to those of the North Pole. However, for the incident angles less than 32° (or larger than 47°), the bias and std values increase as the incident angle decreases (or increases). The reason for this phenomenon is that the average sea ice GMF parameters in the North Pole are used as the sea ice model for the CSCAT, which may not be able to represent the case of the South Pole exactly. Nonetheless, since the GMF difference between the North Pole and South Pole is small, we use the same model for both for the sake of implementation.

Figure 10 summarizes the seasonal correlation of Gaussian fit parameters for the sea ice GMF data in 2019. The increased variation in non-winter months is mainly related to the presence of mixed ice–water pixels, especially in the North Pole. Then, we averaged the Gaussian fit parameters for the North Pole from January to March, and we use the averaged values to represent the distance of the sea ice backscatter to the sea ice GMF for the CSCAT. The results corresponding to the CSCAT operational period (2019–2022) are given in Table 1.

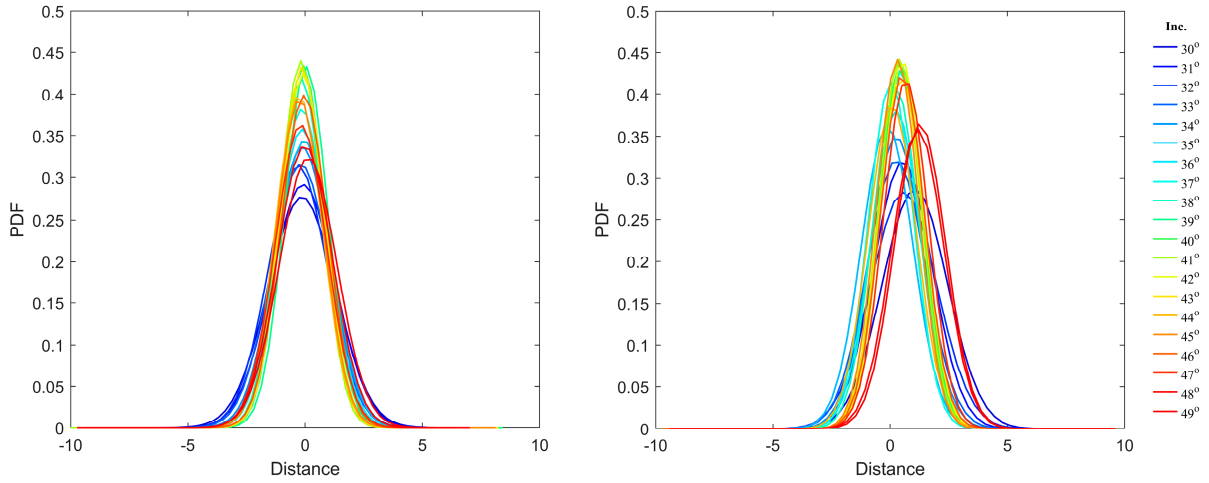


(**a**) (**b**)

**Figure 9.** The Gaussian fit curves of distances of sea ice measured backscatter to its GMF backscatter for different incident angles of CSCAT on 15 January 2019: (**a**) North Pole; (**b**) South Pole.

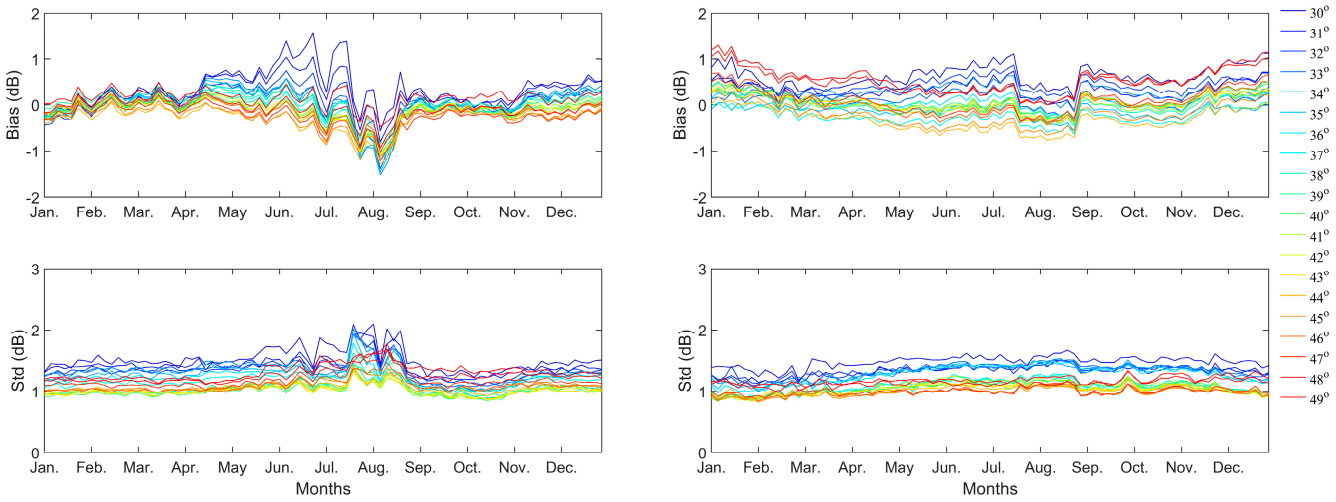


(**a**) (**b**)

**Figure 10.** Gaussian fit parameters in 2019: (**a**) North Pole; (**b**) South Pole.

**Table 1.** Statistical distribution (Gaussian) parameters of sea ice backscatter distances to sea ice GMF.

| Incidence | 2019 | | 2020 | | 2021 | | 2022 | |
|---|---|---|---|---|---|---|---|---|
| | **Bias** | **Std** | **Bias** | **Std** | **Bias** | **Std** | **Bias** | **Std** |
| 30° | 0.11 | 1.46 | 0.10 | 1.59 | 0.17 | 1.86 | 0.14 | 1.91 |
| 31° | 0.12 | 1.40 | 0.09 | 1.49 | 0.04 | 1.72 | 0.21 | 1.79 |
| 32° | −0.06 | 1.34 | −0.02 | 1.56 | −0.10 | 1.86 | 0.11 | 1.84 |
| 33° | −0.05 | 1.32 | 0.01 | 1.57 | −0.05 | 1.97 | 0.06 | 1.78 |
| 34° | 0.06 | 1.32 | 0.11 | 1.60 | 0.25 | 2.02 | 0.24 | 1.84 |
| 35° | 0.07 | 1.25 | 0.09 | 1.55 | 0.20 | 1.97 | 0.19 | 1.8 |
| 36° | 0.04 | 1.20 | 0.02 | 1.59 | −0.09 | 1.98 | 0.03 | 1.77 |
| 37° | −0.02 | 1.12 | −0.12 | 1.42 | −0.16 | 1.68 | −0.07 | 1.58 |
| 38° | −0.03 | 0.99 | −0.13 | 1.17 | −0.21 | 1.34 | −0.19 | 1.34 |
| 39° | 0.16 | 0.98 | −0.05 | 1.05 | −0.16 | 1.23 | −0.07 | 1.24 |

**Table 1.** *Cont.*

| Incidence | 2019 | | 2020 | | 2021 | | 2022 | |
|---|---|---|---|---|---|---|---|---|
| | **Bias** | **Std** | **Bias** | **Std** | **Bias** | **Std** | **Bias** | **Std** |
| 40° | −0.02 | 0.95 | −0.17 | 0.99 | −0.28 | 1.15 | −0.15 | 1.21 |
| 41° | −0.07 | 0.96 | −0.06 | 1.07 | −0.20 | 1.26 | −0.02 | 1.24 |
| 42° | 0.03 | 0.99 | −0.06 | 1.10 | 0.06 | 1.33 | 0.12 | 1.23 |
| 43° | −0.03 | 0.97 | −0.14 | 0.99 | −0.09 | 1.20 | 0.01 | 1.17 |
| 44° | −0.19 | 1.02 | −0.28 | 0.92 | −0.19 | 1.17 | −0.16 | 1.19 |
| 45° | −0.14 | 1.03 | −0.23 | 0.77 | −0.32 | 1.02 | −0.27 | 1.1 |
| 46° | 0.04 | 1.02 | 0.04 | 0.71 | −0.04 | 0.90 | −0.16 | 1.03 |
| 47° | −0.06 | 1.10 | 0.01 | 0.68 | −0.08 | 0.83 | 0.16 | 0.97 |
| 48° | 0.08 | 1.17 | 0.02 | 0.74 | 0.04 | 0.89 | 0.16 | 1.07 |
| 49° | 0.22 | 1.21 | −0.01 | 0.75 | 0.14 | 0.93 | 0.20 | 1.04 |

### *3.4. Squared Distances to GMFs*

The Bayesian algorithm calculates the minimum square distance (or *MLE*, from the maximum likelihood estimator) between the measured backscatters and the sea ice or wind GMF, denoted by $MLE_{\text{ice}}$ and $MLE_{\text{wind}}$, respectively. The probability distribution functions (PDFs) of these two kinds of *MLE* are estimated below.

#### 3.4.1. $MLE_{\text{ice}}$

So far, we have proven that the distance between the sea ice backscatter and its GMF backscatter for each incident angle can be described as a Gaussian function. Then, the *MLE* for sea ice, $MLE_{\text{ice}}$, can be calculated using

$$MLE_{\text{ice}} = \sum_i \left[\left(\sigma^0_{m,i} - \sigma^0_{ice,i} - \mu(\sigma^0_{ice,i})\right)/\text{std}(\sigma^0_{ice,i})\right]^2, i = 1, \ldots, N \quad (2)$$

where $i$ is an index corresponding to a specific incident angle, $N$ (e.g., 2–8) is the number of polarization pairs per WVC, and $\sigma^0_{m,i} - \sigma^0_{ice,i}$ is the distance between the measured backscatter to the sea ice GMF, which can be described by a set of Gaussian variables, i.e., bias $\mu(\sigma^0_{ice,i})$ and standard deviation $\text{std}(\sigma^0_{ice,i})$.

Due to $\left(\sigma^0_{m,i} - \sigma^0_{ice,i} - \mu(\sigma^0_{ice,i})\right)/\text{std}(\sigma^0_{ice,i})$ representing the normalized distance between the sea ice backscatter and its GMF backscatter, Equation (2) can be written as

$$MLE_{\text{ice}} = \sum_i D_i^2, i = 1, \ldots, N \quad (3)$$

where $D_i = \left(\sigma^0_{m,i} - \sigma^0_{ice,i} - \mu(\sigma^0_{ice,i})\right)/\text{std}(\sigma^0_{ice,i})$ is the normalized gaussian variable to satisfy the standard normal distribution with a zero mean and a variance of 1.

Therefore, the sum of squares of $N$ independent variables is subject to a standard normal distribution, $MLE_{\text{ice}}$, which can be modeled using a chi-square distribution with $N$ degrees of freedom. Then, the conditional probability $p(\sigma^0 \mid \text{ice})$ can be expressed as

$$p(\sigma^0|\text{ice}) = \frac{1}{2^{N/2}\Gamma(N/2)} {MLE_{\text{ice}}}^{N/2-1} e^{-MLE_{\text{ice}}/2} \quad (4)$$

As aforementioned, the value of $N$ depends on the across-track WVC number. Figure 11 gives the statical results for $N$ versus the WVC number on 25 January 2019. It can be seen that the distribution of $N$ follows an '$M$' shape, and each WVC contains at most two different pairs of measurements. There are four observation pairs ($N$ = 4) for the nadir swath WVCs (i.e., WVCs 19–26), fewer observation pairs ($N$ < 4) for the outer swath, and more observation pairs ($N$ > 5) for the middle areas on both sides of the swath.

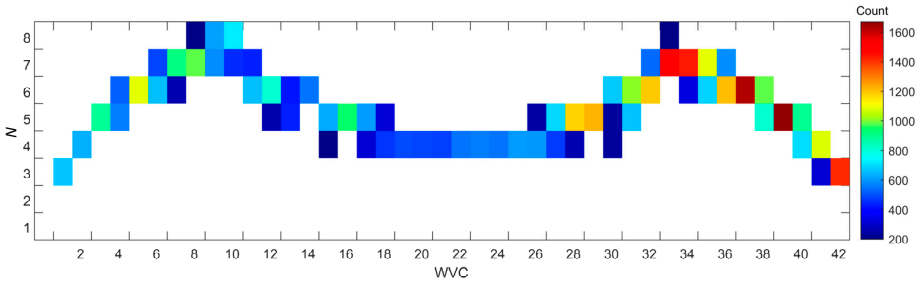


**Figure 11.** The statical results for $N$ per WVC of sea ice for North Pole on 25 January 2019.

Based on the number of measurement pairs for each WVC, the probability distribution of the sea ice backscatter with respect to its GMF under different $N$ is investigated, as shown in Figure 12. Here, the histograms of $MLE_{\text{ice}}$ for all WVCs with the same observation pairs $N$ are evaluated using one day's data. Then, the expected distributions of $MLE_{\text{ice}}$ are verified against the actual measurement distributions. That is, the fitted chi-square distribution curves (red) with $N$ degrees of freedom are superimposed as well as the histogram contours (black). It shows that the majority of the observed $MLE_{\text{ice}}$ distributions are in line with the expected chi-square functions.

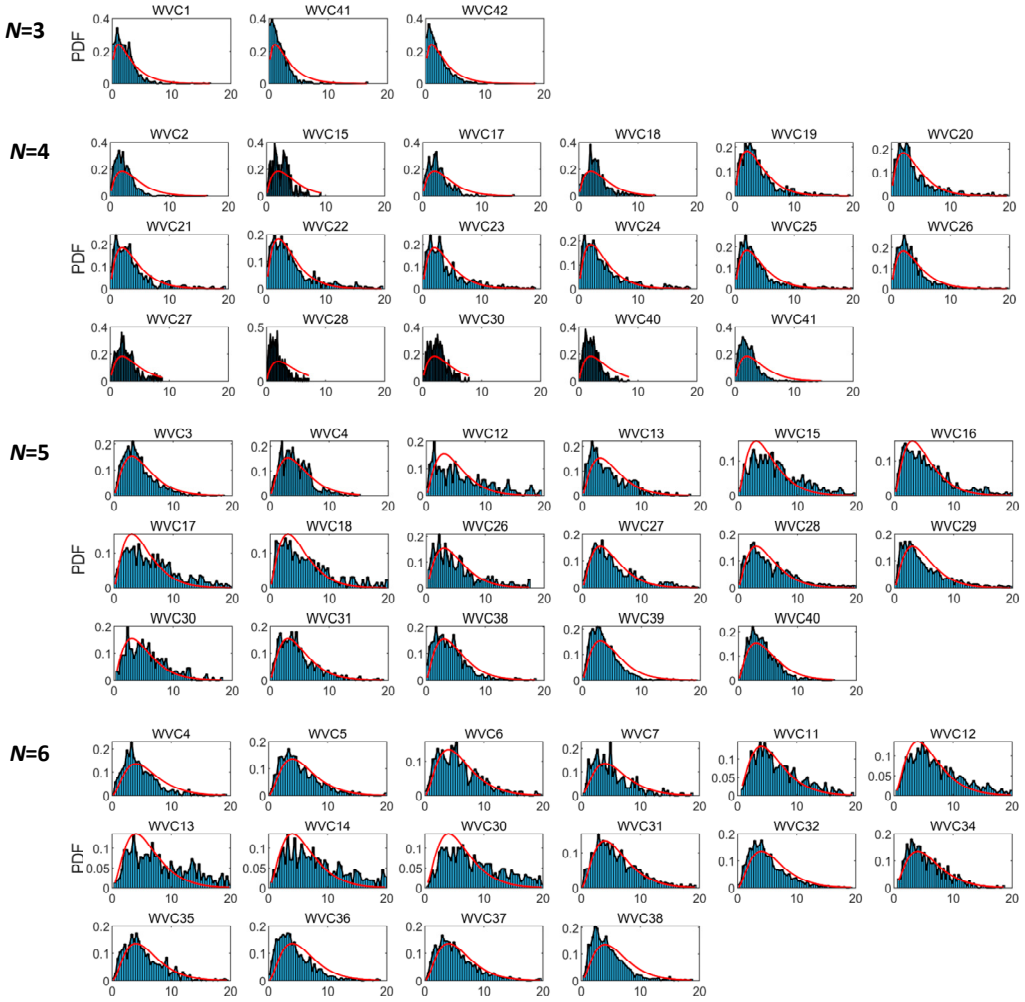


**Figure 12.** *Cont.*

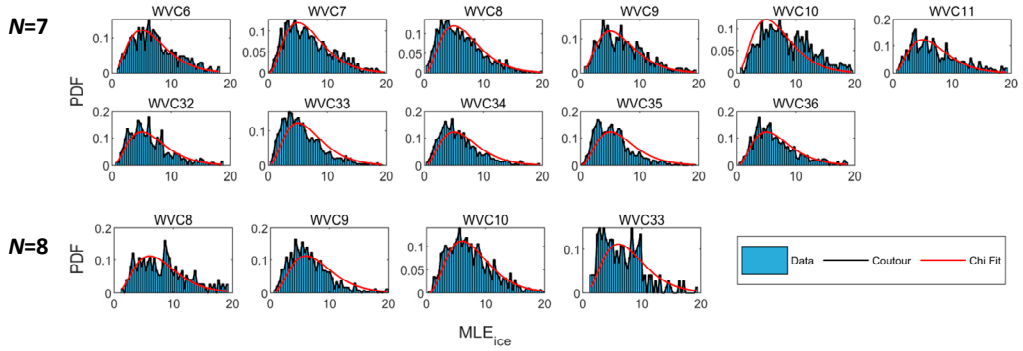


**Figure 12.** The probability distributions of $MLE_{\text{ice}}$ for different $N$ (North Pole, 25 January 2019).

### 3.4.2. $MLE_{\text{wind}}$

The CSCAT wind data processor carries all the necessary information about the ocean wind GMF and its expected error variance. This information is included in the processor's normalized maximum likelihood estimator ($MLE_{\text{wind}}$). In order to maintain consistency with the $MLE_{\text{ice}}$ analysis, the number of measurement pairs $N$ versus the WVC number is calculated for the open water areas of the NSIDC polar stereographic projection maps, as shown in Figure 13. Note that the distribution of $N$ over the open water also satisfies an '$M$' shape. The values of $N$ in the outer and nadir regions of the CSCAT swath are relatively small, with $N$ approximately equal to 4–6. However, the values of $N$ in the middle regions on both sides of the swath are relatively large, with $N$ = 7–8.

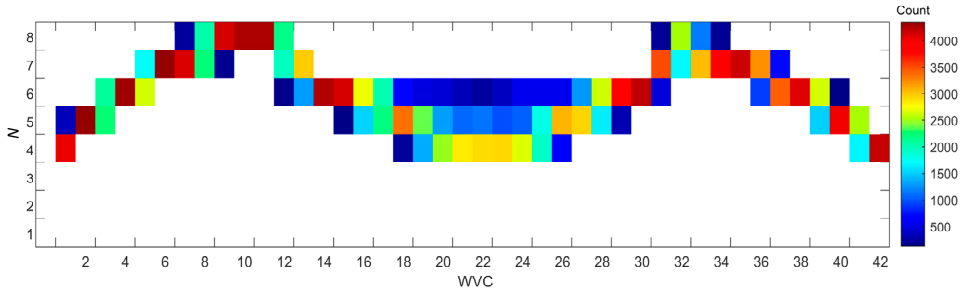


**Figure 13.** The statical results for $N$ per WVC of open water for North Pole on 25 January 2019.

Figure 14 shows the corresponding probability distributions of $MLE_{\text{wind}}$ for different $N$ over the North Pole. We note that these PDFs follow a Gamma distribution. Then, the conditional probability $p(\sigma^0 \mid \text{wind})$ can be expressed by a Gamma distribution with parameters of $a$ and $b$.

$$p(\sigma^0|\text{wind}) = \frac{1}{b^a \Gamma(a)} MLE_{\text{wind}}{}^{a-1} e^{-MLE_{\text{wind}}/b} \quad (5)$$

where $a = N/2$, and the values of parameter $b$ are given in Table 2.

**Table 2.** The values of parameter $b$.

| $N$ | 4 | 5 | 6 | 7 | 8 |
|---|---|---|---|---|---|
| 2019 | 0.45 | 0.35 | 0.30 | 0.25 | 0.23 |
| 2020 | 0.36 | 0.28 | 0.24 | 0.20 | 0.18 |
| 2021 | 0.45 | 0.35 | 0.30 | 0.27 | 0.25 |
| 2022 | 0.99 | 0.77 | 0.66 | 0.55 | 0.51 |


**Figure 14.** The probability distributions of $MLE_{\text{wind}}$ for different $N$ (North Pole, 25 January 2019).

The corresponding Gamma curves for the WVCs with the same $N$ are displayed by red curves in the figure. It is obvious that the majority of the distributions of $MLE_{\text{wind}}$ (see the histograms) show a good agreement with the gamma functions.

### *3.5. Bayesian Posterior Probabilities of Sea Ice*

The KNMI sea ice detection algorithm is based on Bayesian decision rules and needs to calculate a posterior probability of the sea ice. The Bayesian posterior probability formula for the CSCAT sea ice is as follows:

$$p\left(\text{ice}|\sigma^0\right) = \frac{p\left(\sigma^0|\text{ice}\right)p_0(\text{ice})}{p(\sigma^0|\text{ice})p_0(\text{ice}) + p(\sigma^0|\text{wind})p_0(\text{wind})} \tag{6}$$

where

$$p(\sigma^0|\text{ice}) = \frac{1}{2^{N/2}\Gamma(N/2)} {MLE_{\text{ice}}}^{N/2-1} e^{-MLE_{\text{ice}}/2} \tag{7}$$

$$p(\sigma^0|\text{wind}) = \frac{1}{b^a\Gamma(a)} {MLE_{\text{wind}}}^{a-1} e^{-MLE_{\text{wind}}/b},\ a = N/2 \tag{8}$$

and

$$MLE_{\text{ice}} = \sum_i \left[\left(\sigma^0_{m,i} - \sigma^0_{ice,i} - \mu(\sigma^0_{ice,i})\right)/\text{std}(\sigma^0_{ice,i})\right]^2, i = 1, \ldots, N \tag{9}$$

The local prior probabilities for the sea ice and wind are initially set to $p_0(\text{ice}) = p_0(\text{wind}) = 0.50$, and then, they are updated daily based on the posteriors of the previous day as follows:

$$p_0(\text{ice}) = \begin{cases} 0.5, \text{ if } p(\text{ice}|\sigma^0) > 0.30 \\ 0.15, \text{ if } p(\text{ice}|\sigma^0) < 0.30 \end{cases} \tag{10}$$

$$p_0(\text{wind}) = 1 - p_0(\text{ice}) \tag{11}$$

## 4. Results and Discussion

The above sea ice detection algorithm is employed to produce daily polar sea ice posterior probability maps and sea ice masks for the CSCAT mission period (2019–2022). To validate the CSCAT sea ice detection results, quantitative comparisons with passive microwave sea ice concentration are performed in this section.

### *4.1. Sea Ice Mapping*

In this study, the Bayesian posterior probabilities of sea ice derived from the CSCAT data are firstly projected onto the NSIDC Polar Stereographic Projection maps [20]. The top panels of Figures 15 and 16 illustrate the daily sea ice probability maps for six different months, in which the posterior probability ranges from 0% to 100%.

In order to determine the sea ice mask, a threshold must be set for the Bayesian posterior probability to discriminate the sea ice from the open water. Here, a Bayesian posterior probability above 55% is considered as sea ice, and a lower probability is regarded as open water. Then, the resulting sea ice masks are presented in the bottom panels of Figures 15 and 16, respectively. Though only the sea ice mask of one day is shown for each month, the figures clearly illustrate the seasonal variations of sea ice. As expected, the sea ice in the South Pole persists in an opposite variation phase with respect to that of the North Pole.

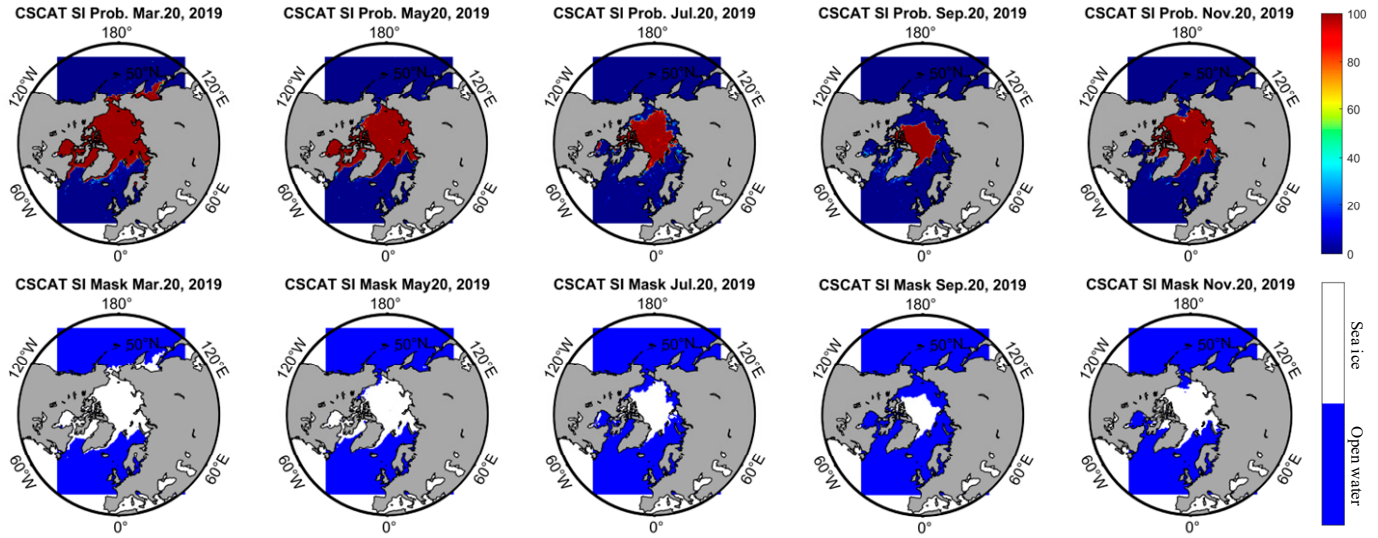


**Figure 15.** Example daily sea ice Bayesian posterior probabilities (**Top Panel**) and sea ice masks (**Bottom Panel**) in North Pole.

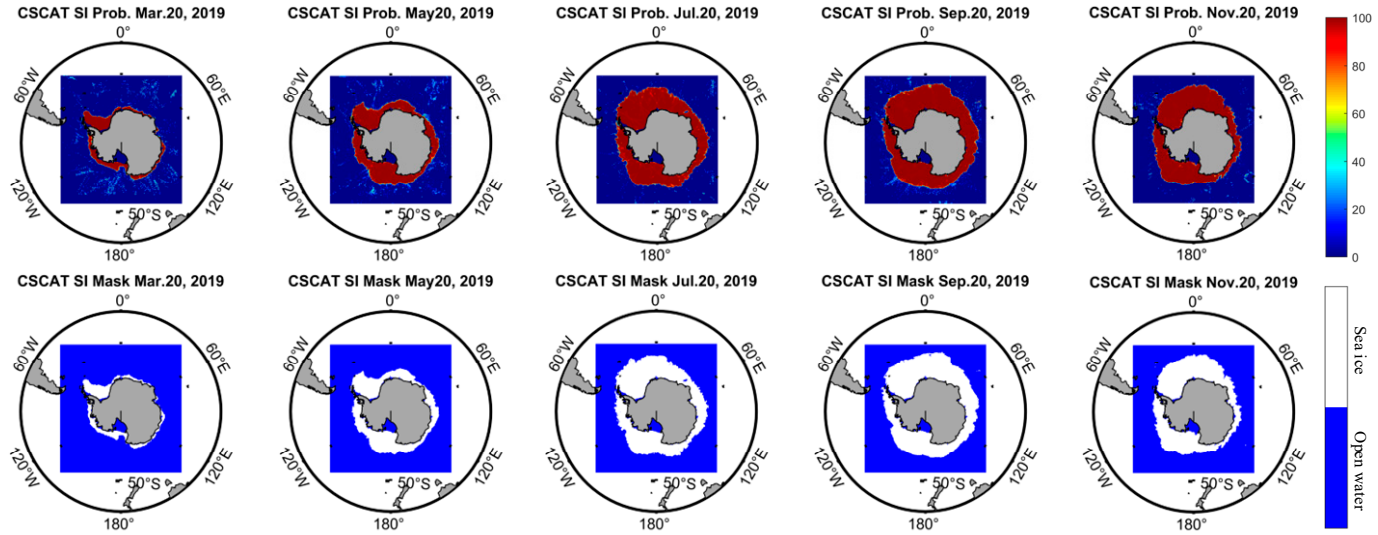


**Figure 16.** Example daily sea ice Bayesian posterior probabilities (**Top Panel**) and sea ice masks (**Bottom Panel**) in South Pole.

### *4.2. Validation*

#### 4.2.1. Validation Sources

The sea ice concentration data derived from passive microwave sensors have more than four decades of data records [21]. Consequently, we use the daily gridded sea ice concentration product as the primary validation reference. Specifically, the sea ice concentration data of the current Special Sensor Microwave Imager (SSMIS) and the Advanced Microwave Scanning Radiometer 2 (AMSR2) are used. These data are generated using the Enhanced NASA Team (NT2) algorithm [22,23]. More relevant information about the sea ice concentration data in the polar stereographic projection is presented in Table 3.

**Table 3.** Sea ice concentration dataset in Polar Stereographic projection.

| Data Source | Sensor | Temporal Coverage | Temporal Sampling | Spatial Coverage | Spatial Sampling |
|---|---|---|---|---|---|
| NOAA NSIDC | SSMIS | January 2015 to present | 1 per day | Global | 25 km |
| | AMSRE | June 2002 to October 2011 | 1 per day | Global | 12.5 km |
| | AMSR2 | July 2012 to present | 1 per day | Global | 12.5 km |
| EUMETSAT OSI SAF | SSMIS | March 2005 to present | 1 per day | Global | 10 km |
| | AMSR2 | September 2016 to present | 1 per day | Global | 10 km |

To validate the CSCAT sea ice detection, comparisons were made with two reference datasets. The first reference dataset is the AMSR2sea ice concentration records provided by the National Oceanic and Atmospheric Administration/National Snow and Ice Data Center (NOAA/NIDC) [24]. Note that this dataset is provided as a polar stereographic projection with a grid size of 12.5 km × 12.5 km, the same as that of the CSCAT sea ice mapping. The second sea ice concentration dataset was provided by the European Meteorological Satellite Organization (EUMETSAT) OSI SAF [25,26]. Both the OSI SAF SSMIS and AMSR2 sea ice concentration datasets have a grid size of 10 km × 10 km.

#### 4.2.2. Sea Ice Edge Comparison

Since both the CSCAT sea ice data and the NSIDC AMSR2 sea ice concentration data were performed on 12.5 km × 12.5 km polar stereographic projection grids, these two types of data were firstly compared with each other. The NSIDC AMSR2 sea ice masks were derived using a specific threshold on their sea ice concentrations.

Firstly, the edge of the CSCAT sea ice mask was carefully validated against the NSIDC AMSR2 sea ice concentration isoline, as shown in Figure 17. In the figure, the sea ice edges of the CSCAT are denoted by red lines, and those of the NSIDC AMSR2 (defined by the sea ice concentration of 15%) are denoted by blue lines. It is obvious that the CSCAT sea ice edges are in a good agreement with the NSIDC AMSR2 sea ice edges.

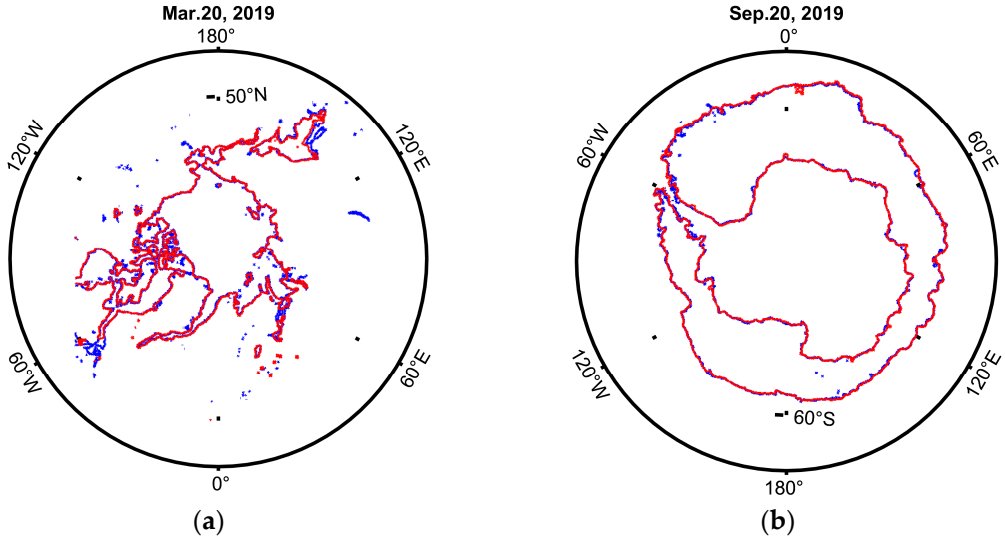


**Figure 17.** Sea ice edge comparison: (**a**) North Pole; (**b**) South Pole. The red lines represent the sea ice edge of CSCAT, and the blue lines denote the NSIDC AMSR2 sea ice concentration 20% isolines.

Secondly, we quantitatively evaluated the difference between the two edges by calculating their statistical distance. The distance from edge to edge was calculated using the Euclidean distance (ED) transformation [27]. Figure 18 shows the mean ED of the sea ice edges between the CSCAT and NSIDC AMSR2 for a set of different sea ice concentration thresholds. Note that the average ED of the sea ice edge between the CSCAT and

NSIDC AMSR2 is the smallest for both the North and South Poles in the case that a sea ice concentration threshold of 15% is used to identify the AMSR2 ice edge.

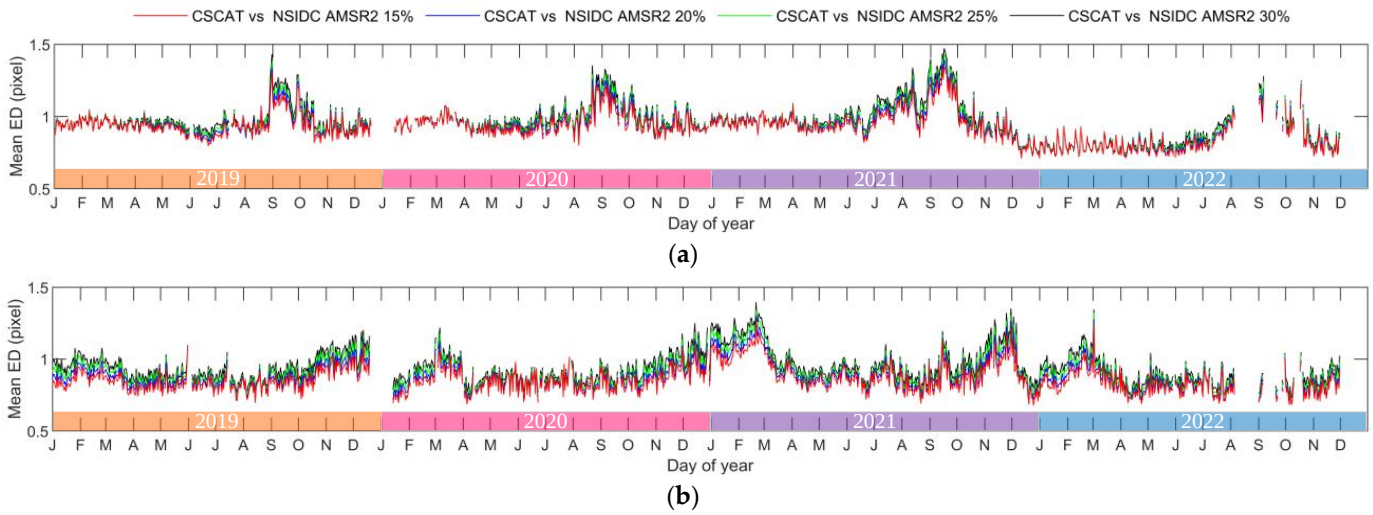


**Figure 18.** The mean ED of sea ice edges between the CSCAT and NSIDC AMSR2 sea ice concentration at different thresholds: (**a**) North Pole; (**b**) South Pole.

By comparing the CSCAT and the NSIDC AMSR2 (i.e., sea ice concentration threshold of 15%) ice edges, the average ED value is basically within 1 pixel in the North Pole. That is, the average ED value is less than 12.5 km. Note that the ED value slightly increases during September (late summer) and October (early autumn), which is larger than 1 pixel but less than 1.5 pixels. This is because of the different capability of the scatterometer and the radiometer in detecting sea ice over the complex sea states. During the ice melting period, the scatterometer-estimated sea ice extent is generally greater than that of the radiometer, while during the ice growing phase the radiometer sea ice extent is generally greater than the CSCAT. In the South Pole, the average ED values are also basically less than 1 pixel.

Overall, the CSCAT sea ice edges estimated by the proposed Bayesian algorithm are closest to the results of the NSIDC AMSR2 with a sea ice concentration threshold of 15%, and the average ED of the sea ice edges is less than 12.5 km.

#### 4.2.3. Sea Ice Extent Comparison

The horizontal dimension of the sea ice cover is usually described by the extent of the sea ice, which can be simply derived by calculating the total area of the sea ice pixels. For the passive microwave sensors, the sea ice range is measured by counting each pixel with a sea ice concentration greater than a certain threshold. The results of the polar ice area of the CSCAT during the mission period (2019–2022) are shown in Figure 19. The NSIDC AMSR2, OSI SAF SSMIS, and OSI SAF AMSR2 sea ice extents are also shown for the comparison.

The plots illustrate the overall variability in the sea ice extent over the four-year period. It is obvious that the sea ice extent of the CSCAT is mostly consistent with the NSIDC AMSR2, followed by the OSI SAF AMSR2, and finally by the OSISAF SSMIS in both hemispheres. This is because the projection of the sea ice maps of the CSCAT and the NSIDC AMSR2 are consistent, such that the pixel-based statistical areas have the smallest deviation. The different grid size results in some uncertainty in the area statistical results for the NSIDC AMSR2 and the OSI SAF AMSR2. In addition, the daily sea ice extent of the South Pole looks smoother than that of the North Pole. This indicates that the sea ice in the North Pole is more sensitive to climate change than the one nearby the South Pole.

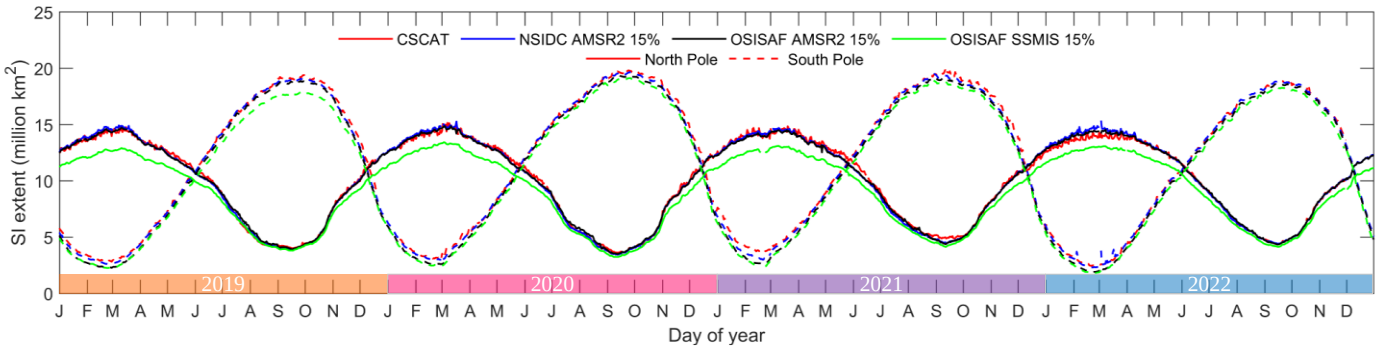


**Figure 19.** Sea ice extent comparison. The solid lines represent the North Pole, and the dashed lines denote the South Pole.

Some quantitative scores of the sea ice extent comparison are given in Table 4. In the table, the absolute mean and standard deviation of the difference between the CSCAT-derived sea ice extent and the radiometer-derived sea ice extent at various thresholds are calculated. Again, the results show that the sea ice extent difference between the CSCAT and the radiometer is smallest for both the North and South Poles when a sea ice concentration threshold of 15% is used. Moreover, the absolute mean and standard deviation of the CSCAT versus NSIDC AMSR2 are smallest. This is due to the fact that the CSCAT and NSIDC AMSR2 ice extents are both mapped on the same grids.

**Table 4.** Statistics of the sea ice extent comparisons between CSCAT and passive microwave.

| Region | Comparisons | Sea Ice Concentration Threshold | Absolute Mean ($10^6$ km$^2$) | | | | Standard Deviation ($10^6$ km$^2$) | | | |
|---|---|---|---|---|---|---|---|---|---|---|
| | | | 2019 | 2020 | 2021 | 2022 | 2019 | 2020 | 2021 | 2022 |
| North Pole | CSCAT vs. NSIDC AMSR2 | 15% | 0.02 | 0.06 | 0.16 | 0.17 | 0.68 | 0.22 | 0.24 | 0.31 |
| | | 20% | 0.03 | 0.11 | 0.21 | 0.11 | 0.68 | 0.22 | 0.25 | 0.30 |
| | | 25% | 0.08 | 0.16 | 0.27 | 0.06 | 0.68 | 0.22 | 0.25 | 0.30 |
| | | 30% | 0.12 | 0.21 | 0.31 | 0.01 | 0.68 | 0.22 | 0.25 | 0.30 |
| | CSCAT vs. OSI SAF AMSR2 | 15% | 0.02 | 0.04 | 0.18 | 0.11 | 0.68 | 0.21 | 0.22 | 0.21 |
| | | 20% | 0.08 | 0.15 | 0.29 | 0.00 | 0.68 | 0.21 | 0.24 | 0.21 |
| | | 25% | 0.19 | 0.25 | 0.39 | 0.09 | 0.68 | 0.22 | 0.26 | 0.22 |
| | | 30% | 0.29 | 0.35 | 0.50 | 0.19 | 0.68 | 0.24 | 0.28 | 0.24 |
| | CSCAT vs. OSI SAF SSMIS | 15% | 0.85 | 0.88 | 1.02 | 0.82 | 0.87 | 0.44 | 0.44 | 0.34 |
| | | 20% | 0.85 | 0.88 | 1.02 | 0.83 | 0.87 | 0.44 | 0.44 | 0.34 |
| | | 25% | 0.94 | 0.98 | 1.12 | 0.92 | 0.86 | 0.43 | 0.43 | 0.33 |
| | | 30% | 1.06 | 1.11 | 1.26 | 1.05 | 0.86 | 0.44 | 0.43 | 0.33 |
| South Pole | CSCAT vs. NSIDC AMSR2 | 15% | 0.19 | 0.14 | 0.29 | 0.03 | 0.20 | 0.23 | 0.27 | 0.18 |
| | | 20% | 0.26 | 0.21 | 0.36 | 0.09 | 0.21 | 0.25 | 0.28 | 0.19 |
| | | 25% | 0.31 | 0.28 | 0.43 | 0.15 | 0.22 | 0.27 | 0.30 | 0.20 |
| | | 30% | 0.37 | 0.34 | 0.50 | 0.21 | 0.23 | 0.29 | 0.31 | 0.21 |
| | CSCAT vs. OSI SAF AMSR2 | 15% | 0.46 | 0.42 | 0.57 | 0.34 | 0.18 | 0.22 | 0.30 | 0.16 |
| | | 20% | 0.63 | 0.61 | 0.78 | 0.51 | 0.23 | 0.29 | 0.34 | 0.18 |
| | | 25% | 0.78 | 0.78 | 0.97 | 0.66 | 0.28 | 0.37 | 0.40 | 0.23 |
| | | 30% | 0.93 | 0.95 | 1.17 | 0.81 | 0.34 | 0.46 | 0.48 | 0.28 |
| | CSCAT vs. OSI SAF SSMIS | 15% | 0.93 | 0.66 | 0.82 | 0.60 | 0.35 | 0.21 | 0.27 | 0.16 |
| | | 20% | 0.93 | 0.67 | 0.82 | 0.60 | 0.35 | 0.21 | 0.27 | 0.16 |
| | | 25% | 1.08 | 0.85 | 1.01 | 0.75 | 0.39 | 0.28 | 0.32 | 0.20 |
| | | 30% | 1.27 | 1.08 | 1.26 | 0.95 | 0.44 | 0.36 | 0.38 | 0.26 |

In a word, the distributions of the daily sea ice extent from the CSCAT and NSIDC AMSR2 are basically consistent for both the North and South Poles. The overall standard deviation difference between both is less than $0.3 \times 10^6$ km$^2$.

## 5. Conclusions

Scatterometers are active microwave sensors used for oceanic applications (including ocean surface wind and sea ice). This paper takes the first spaceborne Ku-band rotating fan beam scatterometer, the CSCAT, as an example to explore the effectiveness of this new scatterometer in polar sea ice detection. A Bayesian approach with consideration of the characteristics of multiple incidence angles and dual polarization of the CSCAT is established. Note that the algorithm is different from our previous work, which only uses the data at an incidence angle of 40° for sea ice detection [15,16]. Based on the observation geometry of the CSCAT, the CSCAT backscatter space is defined firstly. The GMF of sea ice is derived from the observed sea ice backscatter, and it is described in the CSCAT backscatter space. Then, the Bayesian algorithm is implemented by using the squared distances between the measured backscatter and the GMFs of sea ice and ocean surface wind. With the developed algorithm, the daily sea ice posterior probabilities and the sea ice masks (by setting a threshold of 55% for the Bayesian posterior probability) are produced for the mission period (2019–2022). To validate the CSCAT sea ice detection results, comparisons with three reference data sets, namely the NSIDC AMSR2 sea ice concentration, the OSI SAF SSMIS sea ice concentration, and the OSI SAF AMSR2 sea ice concentration, are performed from 2019 to 2022. Firstly, the edge of the CSCAT sea ice mask has been carefully validated against the NSIDC AMSR2 sea ice concentration isoline, and the results show that the CSCAT sea ice edges are in a good agreement with the NSIDC AMSR2 sea ice edges. The difference between the two edges is evaluated quantitatively using the ED. It is found that the CSCAT sea ice edges are closest to the results of the NSIDC AMSR2 with a sea ice concentration threshold of 15%, and the average ED of sea ice edges is less than 12.5 km. Secondly, the sea ice extents derived from the CSCAT are compared with that of the NSIDC AMSR2, OSI SAF SSMIS, and OSI SAF AMSR2 with different sea ice concentration thresholds. The results show that the sea ice extent of the CSCAT is mostly consistent with that of the NSIDC AMSR2, followed by the OSI SAF AMSR2, and finally by the OSISAF SSMIS. The reason for this is that the sea ice maps of the CSCAT and NSIDC AMSR2 share the same projection, thus the pixel-based statistical extent has the smallest deviation. The overall difference of the sea ice extent between the CSCAT and NSIDC AMSR2 is less than $0.3 \times 10^6$ km$^2$. The validation demonstrates the effectiveness of the established sea ice detection approach for the CSCAT and proves that the rotating fan beam scatterometer is an effective sensor for polar monitoring.

**Author Contributions:** Conceptualization, L.L. and X.D.; methodology, L.L. and W.L.; software, L.L.; validation, L.L.; formal analysis, L.L.; investigation, L.L.; resources, S.L.; data curation, L.L.; writing—original draft preparation, L.L.; writing—review and editing, L.L. and W.L.; visualization, L.L.; supervision, X.D.; project administration, S.L. and L.L.; funding acquisition, L.L. All authors have read and agreed to the published version of the manuscript.

**Funding:** This research is supported by the Fundamental Research Funds for the Central Universities (Grant No. 2022YQJD22) and the National Natural Science Foundation of China (Grant No. 41806209).

**Data Availability Statement:** The CSCAT scientific product used in the study is available from the NSOAS website: https://osdds.nsoas.org.cn/MarineDynamic accessed on 1 September 2022. The NSIDC AMSR2 sea ice concentration dataset is available at https://nsidc.org/data/ae_si12/versions/3 accessed on 7 August 2023. The EUMETSAT OSI SAF SSMIS and the AMSR2 sea ice concentration dataset is available at https://osi-saf.eumetsat.int/products/osi-401-d accessed on 7 August 2023 and https://osi-saf.eumetsat.int/products/osi-408-a accessed on 7 August 2023.

**Acknowledgments:** We acknowledge the support of the NSOAS and CFOSAT team in providing the data, status, and mission information. The passive microwave datasets provided by the NSIDC and EUMETSAT OSI SAF are much appreciated.

**Conflicts of Interest:** The authors declare no conflict of interest.

## References

1. Long, D.G. Polar Applications of Spaceborne Scatterometers. *IEEE J. Sel. Top. Appl. Earth Obs. Remote Sens.* **2017**, *10*, 2307–2320. [CrossRef] [PubMed]
2. Singh, S.; Tiwari, R.K.; Sood, V.; Kaur, R.; Prashar, S. The Legacy of Scatterometers: Review of applications and perspective. *IEEE Geosci. Remote Sens. Mag.* **2022**, *10*, 39–65. [CrossRef]
3. Verspeek, J. *Sea Ice Classification Using Bayesian Statistics*; KNMI: De Bilt, The Netherlands, 2006.
4. Liu, J.; Lin, W.; Dong, X.; Lang, S.; Yun, R.; Zhu, D.; Zhang, K.; Sun, C.; Mu, B.; Ma, J.; et al. First Results From the Rotating Fan Beam Scatterometer Onboard CFOSAT. *IEEE Trans. Geosci. Remote Sens.* **2020**, *58*, 8793–8806. [CrossRef]
5. Daily Arctic and Antarctic Sea Ice Extents and Normalized Backscatter. Available online: https://scatterometer.knmi.nl/ice_extents/ (accessed on 7 August 2023).
6. Li, Z.; Verhoef, A.; Stoffelen, A.; Shang, J.; Dou, F. First Results from the WindRAD Scatterometer on Board FY-3E: Data Analysis, Calibration and Wind Retrieval Evaluation. *Remote Sens.* **2023**, *15*, 2087. [CrossRef]
7. Zhai, X.; Wang, Z.; Zheng, Z.; Xu, R.; Dou, F.; Xu, N.; Zhang, X. Sea Ice Monitoring with CFOSAT Scatterometer Measurements Using Random Forest Classifier. *Remote Sens.* **2021**, *13*, 4686. [CrossRef]
8. Xu, C.; Wang, Z.; Zhai, X.; Lin, W.; He, Y. SVM-Based Sea Ice Extent Retrieval Using Multisource Scatterometer Measurements. *Remote Sens.* **2023**, *15*, 1630. [CrossRef]
9. Remund, Q.P.; Long, D.G. Sea ice extent mapping using Ku band scatterometer data. *J. Geophys. Res. Ocean.* **1999**, *104*, 11515–11527. [CrossRef]
10. Anderson, H.; Long, D.G. Sea ice mapping method for SeaWinds. *IEEE Trans. Geosci. Remote Sens.* **2005**, *43*, 647–657. [CrossRef]
11. Near Real-Time Sea Ice Discrimination Using SeaWinds on QUIKSCAT. Available online: https://cdn.knmi.nl/system/data_center_publications/files/000/068/084/original/sea_ice_osi_saf_final_report.pdf?1495621021 (accessed on 7 August 2023).
12. Rivas, M.B.; Stoffelen, A. New Bayesian Algorithm for Sea Ice Detection with QuikSCAT. *IEEE Trans. Geosci. Remote Sens.* **2011**, *49*, 1894–1901. [CrossRef]
13. Rivas, M.B.; Verspeek, J.; Verhoef, A.; Stoffelen, A. Bayesian Sea Ice Detection with the Advanced Scatterometer ASCAT. *IEEE Trans. Geosci. Remote Sens.* **2012**, *50*, 2649–2657. [CrossRef]
14. Otosaka, I.; Rivas, M.B.; Stoffelen, A. Bayesian Sea Ice Detection with the ERS Scatterometer and Sea Ice Backscatter Model at C-Band. *IEEE Trans. Geosci. Remote Sens.* **2018**, *56*, 2248–2254. [CrossRef]
15. Liu, L.; Dong, X.; Lin, W.; Lang, S.; Wang, L. Polar Sea Ice Detection with the CFOSAT Scatterometer. In Proceedings of the IEEE International Geoscience and Remote Sensing Symposium, Brussels, Belgium, 11–16 July 2021.
16. Liu, L.; Zhai, H.; Dong, X.; Zhao, F. SEA ICE Extent Retrieval with Ku-Band Rotating Fan Beam Scatterometer Data. In Proceedings of the IEEE International Geoscience and Remote Sensing Symposium, Kuala Lumpur, Malaysia, 17–22 July 2022.
17. Li, Z.; Verhoef, A.; Stoffelen, A. Bayesian Sea Ice Detection Algorithm for CFOSAT. *Remote Sens.* **2022**, *14*, 3569. [CrossRef]
18. Lin, W.; Dong, X.; Portabella, M.; Lang, S.; He, Y.; Yun, R.; Wang, Z.; Xu, X.; Zhu, D.; Liu, J. A Perspective on the Performance of the CFOSAT Rotating Fan-Beam Scatterometer. *IEEE Trans. Geosci. Remote Sens.* **2018**, *57*, 627–639. [CrossRef]
19. Yun, R.; Dong, X.; Liu, J.; Lin, W.; Zhu, D.; Ma, J.; Lang, S.; Wang, Z. CFOSAT Rotating Fan-beam Scatterometer Backscatter Measurement Processing. *Earth Space Sci.* **2021**, *8*, 1–18. [CrossRef]
20. A Guide to NSIDC's Polar Stereographic Projection, National Snow and Ice Data Center. Available online: https://nsidc.org/data/user-resources/help-center/guide-nsidcs-polar-stereographic-projection (accessed on 7 August 2023).
21. Sandven, S.; Spreen, G.; Heygster, G.; Girard-Ardhuin, F.; Farrell, S.; Dierking, W.; Allard, R. Sea Ice Remote Sensing—Recent Developments in Methods and Climate Data Sets. *Surv. Geophys.* **2023**, *44*, 1–37. [CrossRef]
22. Markus, T.; Cavalieri, D.J. An enhancement of the NASA Team sea ice algorithm. *IEEE Trans. Geosci. Remote Sens.* **2000**, *38*, 1387–1398. [CrossRef]
23. Markus, T.; Cavalieri, D.J. The AMSR-E NT2 Sea Ice Concentration Algorithm: Its Basis and Implementation. *J. Remote Sens. Soc. Jpn.* **2009**, *29*, 216–225. [CrossRef]
24. AMSR-E/AMSR2 Unified L3 Daily 12.5 km Brightness Temperatures, Sea Ice Concentration, Motion & Snow Depth Polar Grids V001. Version 1. Available online: https://catalog.data.gov/dataset/amsr-e-amsr2-unified-l3-daily-12-5-km-brightness-temperatures-sea-ice-concentration-motion (accessed on 7 August 2023).
25. OSI SAF Global Sea Ice Concentration (SSMIS), OSI-401-d. Available online: https://osi-saf.eumetsat.int/products/osi-401-d (accessed on 7 August 2023).

26. OSI SAF Global Sea Ice Concentration (AMSR-2), OSI-408-a. Available online: https://osi-saf.eumetsat.int/products/osi-408-a (accessed on 7 August 2023).
27. Contour-to-Contour Distance. Available online: https://www.mathworks.com/matlabcentral/fileexchange/75551-contour-to-contour-distance (accessed on 7 August 2023).